High performance piezoelectric vibration energy harvesting by electrical resonant frequency tuning

David Gibus, Adrien Morel, Pierre Gasnier, Adrien Ameye, Adrien Badel

▶ **To cite this version:**

David Gibus, Adrien Morel, Pierre Gasnier, Adrien Ameye, Adrien Badel. High performance piezoelectric vibration energy harvesting by electrical resonant frequency tuning. Smart Materials and Structures, 2022, 31 (12), pp.125012. 10.1088/1361-665X/ac9d74 . hal-03845270

HAL Id: hal-03845270
https://hal.science/hal-03845270v1

Submitted on 9 Nov 2022

HAL is a multi-disciplinary open access archive for the deposit and dissemination of scientific research documents, whether they are published or not. The documents may come from teaching and research institutions in France or abroad, or from public or private research centers.

L'archive ouverte pluridisciplinaire **HAL**, est destinée au dépôt et à la diffusion de documents scientifiques de niveau recherche, publiés ou non, émanant des établissements d'enseignement et de recherche français ou étrangers, des laboratoires publics ou privés.

High performance piezoelectric vibration energy harvesting by electrical resonant frequency tuning

David GIBUS[1,*], Adrien MOREL[1], Pierre GASNIER[2], Adrien AMEYE[1,2] and Adrien BADEL[1]

[1] SYMME, Université Savoie Mont-Blanc, F-74000, Annecy, France
[2] Université Grenoble Alpes, CEA, LETI, MINATEC, F-38000 Grenoble, France
*david.gibus@univ-smb.fr

Abstract

Extending the frequency bandwidth of vibration energy harvesters (VEH) that power wireless sensor nodes is of scientific and industrial interest. In this aim, electrical methods to tune the resonant frequency of piezoelectric harvesters with strong electromechanical coupling coefficients have been developed. In this work, we provide guidelines for designing such strongly coupled VEH and present a broadband harvester with high normalized power density (NPD). Through an analytical model, we explain how the coupling coefficient k^2 and the quality factor Q_m of a cantilever can be jointly maximized, thereby maximizing the figure of merit $k_e^2 Q_m$. The proposed cantilever prototype made of PZN-5.5PT and aluminum offers one of the best coupling coefficients among the state-of-the-art (k^2=49.8%) and a high quality factor (Q_m=140). Associated to an appropriate tunable electrical interface (short-circuit synchronous electric charge extraction in our case), the prototype exhibits a normalized power density of 12.0 mW/g²/cm³ and a frequency bandwidth (BW) of 36.0 % (56.5 Hz around 157 Hz) at 0.34 m/s² with a tunable electrical interface: the short-circuit synchronous electric charge extraction. This represents the highest product NPWxBW from state of the art.

Nomenclature

M_t	Mass of the proof mass	L_b	Beam length
I_t	Rotary inertia of the proof mass according to its center of gravity	D_t	Distance between the free end of the beam and the center of gravity of the proof mass
L_m	Proof mass length	H_m	Proof mass height
f_{sc}	Short-circuit resonant frequency of the harvester	f_{oc}	Open-circuit resonant frequency of the harvester
δf_{rel}	Relative frequency tuning range between f_{sc} and f_{oc}	a , b	Coefficients that define the beam mode shape expression
k_{31}^2	Electromechanical coupling coefficient of the piezoelectric material	k_{e31}^2	Expedient coupling coefficient of the piezoelectric material $k_{e31}^2 = k_{31}^2/(1-k_{31}^2)$
k^2	Global electromechanical coupling coefficient of the piezoelectric harvester	k_e^2	Alternative coupling coefficient of the piezoelectric harvester $k_e^2 = k^2/(1-k^2)$
Y_s	Young modulus of the substrate	c_{11}	Linear elastic equivalent coefficient of the piezoelectric material
YI	Linear bending stiffness of the beam	B	Beam and mass width
η	Mechanical loss factor	Q_s	Quality factor of the substrate

Q_p	Quality factor of the piezoelectric material at short-circuit resonance	Q_m	Quality factor of the harvester at short-circuit resonance
h_s	Thickness of the substrate	h_p	Thickness of each piezoelectric patch
$\frac{h_p}{h_s}\Big\|_{k_e^2}^{\text{opt}}$	Optimal thickness ratio that maximize k_e^2	$\frac{h_p}{h_s}\Big\|_{k_e^2 Q_m}^{\text{opt}}$	Optimal thickness ratio that maximize $k_e^2 Q_m$
ω	Vibration pulsation	$\mathcal{R}_T$	Thickness factor in the expression of k_e^2
r	Generalized spatial coordinate	$\mathcal{R}_L$	Length factor in the expressions of k_e^2 and $k_e^2 Q_m$
v	Voltage accross the piezoelectric electrodes	$\mathcal{R}_Q$	Factor in the expression of $k_e^2 Q_m$
B_f	Forcing term	M	Equivalent mass
K	Equivalent linear stiffness	K_2	Nonlinear stiffness
Θ	Linear coupling term	Θ_2	Nonlinear coupling term
b_1	Linear structural loss coefficient	b_2	Second order structural loss coefficient
C_p	Equivalent clamped capacitance	R_{load}	Resistive load
w_B	Base displacement of the beam	d_1	Linear dielectric loss coefficient
$\dot{\square}$	Temporal derivative		

1. Introduction

Vibrational energy harvesting is often envisioned to power autonomous wireless sensors nodes. In particular, it could be useful in environments where batteries are difficult to change [1]. However, a major obstacle to large-scale industrialization of vibrational energy harvesters (VEH) is their low operating frequency band. To address this issue, a solution is to use power management circuits capable of tuning the resonant frequency of piezoelectric VEH [2]. Such circuits based on synchronous electric charge extraction (SECE) [3,4] and synchronized switch harvesting on inductor (SSHI) [5] have shown interesting performances on strongly coupled VEHs. Moreover, fully autonomous integrated circuit have been recently designed in the literature [6,7] and offer interesting opportunities for this approach. These autonomous circuits are able to tune automatically the resonant frequency with low power consumption (<1 µW) on a relatively large frequency band (10-30% of the resonant frequency) when they are associated to VEHs with strong electromechanical couplings. Since the impact of the circuit on the VEH dynamics is increasing with the coupling, the electromechanical coupling coefficient k^2 of the piezoelectric harvesters needs to be maximized in order to increase the frequency tuning range. Nevertheless, the electromechanical coupling coefficient of most harvesters of the literature remains relatively weak ($k^2 < 20\%$) [8], and few guidelines are given to design very strongly coupled harvesters [9]. Moreover, the quality factor Q_m is rarely considered in the sizing methods even though it is an essential lever to maximize the harvested power. The present paper therefore introduces a method for designing strongly coupled piezoelectric cantilevers. As a result, one of the best performing VEHs among the state-of-the-art in terms of frequency bandwidth and normalized power density is presented.

Few strongly coupled piezoelectric harvesters have already been presented in the state-of-the-art for the purpose of resonant frequency tuning by electrical methods. Wu *et al.* [10] and Charnergie [11] proposed, respectively in 2006 and 2007, electrical circuits for the resonant frequency tuning of piezoelectric VEHs that were moderately coupled. Since the electromechanical coupling coefficients of the VEHs were moderate, frequency tuning ranges were limited (less than 4% of the center frequency). Regarding the dedicated design of VEH, Ahmed-Seddik *et al.* introduced in 2012 an innovative tapered cantilever employing PZN-PT material [12]. Their VEH demonstrated a coupling coefficient $k^2$of 50 % and 32.7 % of frequency bandwidth [13] but no design method was proposed and compared to experiments. In addition, the VEH demonstrated a low quality factor and its intricate mounting method makes it unsuitable for industrial applications. In 2014, Badel and Lefeuvre presented a VEH based on PZN-PT material that reached an electromechanical coupling coefficient k^2 of 53 % [9]. Their device was a cantilever with a long proof mass that could theoretically have a frequency bandwidth of 45% with the Frequency

Tunable SECE (FT-SECE) technique. Despite these interesting performances, their study did not present optimization methods and experimental results under vibration. In 2018, Morel *et al.* presented the Short-Circuit SECE (SC-SECE) technique that allowed to reach 43.5 % frequency bandwidth with a similar PZN-PT based cantilever ($k^2 = 32$ %) but no recommendations have been made for the design of the cantilever [3]. The same year, Cai and Manoli [7] used a commercially available beam with a moderate electromechanical coupling coefficient ($k^2 < 10$ %) to experiment an innovative integrated circuit. Even if the proposed electrical technique had a notable influence on the experienced bandwidth, the interesting bandwidth (9.0 % of the center frequency) was partly due to the low quality factor ($Q_m = 28$), which lead to a low power density solution.

Regarding the optimization of piezoelectric cantilevers, the present authors demonstrated in 2020, theoretically and experimentally, that bimorphs with long proof mass are among the best structures to maximize the global coupling coefficient [8]. A strongly coupled PZT-based cantilever ($k^2 = 16.4\%$) was presented and reached 18 % frequency bandwidth with a fully integrated circuit presented by Morel *et al.* [6]. More recently, in 2021, Zhao *et al.* presented the design of a PZT-5H cantilever ($k^2 = 14$ %) that allowed a frequency bandwidth of 12.8 % with a tunable Phase-Shift Parallel SSHI (PS-PSSHI) circuit [5]. However, while we show in the present work that the substrate material stiffness has a significant impact on the design of a piezoelectric cantilever, the latter was neglected in the cantilever optimization performed by Zhao *et al.* Finally, as an alternative to cantilever-based VEH for electrical resonant frequency tuning, a flextensionnal structure with a strong coupling coefficient ($k^2 =$ 11.5 %) was proposed by Kuang *et al.* in 2020 [14]. While flextensionnal structures seem interesting because the piezoelectric material is only stressed in compression and with 33-mode (which is generally more coupled than 31-mode stressed in cantilevers), they generally have a high resonant frequency and the values of k^2 reached are low compared to the coupling coefficient of the materials.

In addition to the coupling coefficient k^2 that allows to maximize the frequency bandwidth, the quality factor Q_m should be considered in the optimization of the piezoelectric VEH as it is directly related to the amount of energy harvested [15]. Its maximization involves minimizing the system losses. Nevertheless, none of the above works that introduced guidelines to maximize the k^2 [5,8,12] considered the materials losses in the design process and addressed the conjoint maximization of the electromechanical coupling coefficient k^2 and the mechanical quality factor Q_m (i.e. the figure of merit $k_e^2 Q_m$ with $k_e^2 = k^2/(1-k^2)$). Moreover, none of them is dedicated to very strongly coupled materials and addressed the choice of substrate materials. In this paper, we therefore present a design method based on modeling and simulations to maximize the figure of merit $k_e^2 Q_m$ of strongly coupled bimorphs in order to tune their resonant frequency.

The next section introduces theoretical guidelines based on analytical expressions of the expedient coupling coefficient k_e^2 and of the quality factor Q_m of a piezoelectric cantilever. The third section discusses the specific optimization of such a cantilever conducted using the present model, losses measurements and 3D FEM simulations. The last section presents a strongly coupled cantilever exhibiting wide frequency bandwidth and high normalized power density. Its experimental validation is detailed with an electrical resonant frequency tuning technique and its performances are compared to VEH from the state-of-the-art.

2. Modelling

This section is dedicated to the device presentation and its optimization from an analytical model. We firstly show in which manner increasing the electromechanical coupling coefficient of piezoelectric harvesters increases the abilities to tune their resonant frequency. Guidelines are secondly offered in order to maximize the global coupling coefficient of a piezoelectric cantilever through its expression. Thirdly, as the quality factor Q_m greatly influence the harvested power, an expression of Q_m is derived and studied. Finally, as k_e^2 influences the bandwidth and $Q_m$influences the harvested power, $k_e^2 Q_m$ is an important figure of merit for piezoelectric vibration energy harvesters. For this reason, the maximization of the $k_e^2 Q_m$ figure of merit is discussed at the end of this section.

It should be noted that a linear behaviour of the piezoelectric VEH is considered in this section. As shown in sections 3 and 4, piezoelectric materials exhibit non-linear behaviour under vibrational excitation. Nevertheless, considering linear behaviour of the VEH at low excitation levels remains necessary for the design process.

2.1. The interest of the electromechanical coupling

Considering resonant frequency tuning by electrical methods, the influence of the electromechanical coupling coefficient k^2 on the expected frequency bandwidth is observable with the computation of the short circuit resonant

frequency f_{sc} and the open circuit resonant frequency f_{oc}. Indeed, some electrical techniques (e.g. SC-SECE or resistive and capacitive tuning) are able to tune the resonant frequency of strongly coupled VEHs in the range between f_{sc} and f_{oc} as a first approximation when $k_e^2 Q_m$ is sufficiently large (e.g. $k_e^2 Q_m > 2$ for resistive and capacitive tuning [16]). The resonant frequency can even be tuned a little further than f_{sc} and f_{oc} by some techniques such as SC-SECE [3]. As f_{oc} is a function of f_{sc} and of the alternative coupling coefficient ${k_e}^2$ as described in equation (1), δf_{rel} (i.e. the relative minimum range of frequencies where the resonant frequencies can be tuned) only depends on the alternative coupling coefficient k_e^2 as expressed in (2), where f_c is the central frequency given by $(f_{oc} + f_{sc})/2$.

$$f_{oc} = f_{sc}\sqrt{1 + k_e^2} \tag{1}$$

$$\delta f_{rel} = \frac{\delta f_{tuning}}{f_c} = 2\frac{f_{oc} - f_{sc}}{f_{oc} + f_{sc}} = 2\frac{\sqrt{1+k_e^2}-1}{\sqrt{1+k_e^2}+1} = \frac{2k_e^2}{\left(\sqrt{1+k_e^2}+1\right)^2} \tag{2}$$

The alternative coupling coefficient k_e^2 is a way to express the electromechanical coupling of piezoelectric devices that directly depends on the global electromechanical coupling coefficient k^2 as expressed in (3). k^2 is inferior to 1 while k_e^2 can be greater than 1 (if $k^2 > 50$ %).

$$k_e^2 = \frac{k^2}{1 - k^2} \tag{3}$$

While k^2 was commonly used in the literature, k_e^2 is preferably used in the present work as a figure of merit. Indeed k_e^2 is easier to express and to study and is directly related to the relative frequency tuning range. Furthermore, the figure of merit $k_e^2 Q_m$ is the relevant one (with comparison with $k^2 Q$) for piezoelectric devices as it provides reference values [17] . For the convenience of readers, Table 1 reports few values corresponding values for k^2 and k_e^2

Table 1: Corresponding values of k^2 and k_e^2 . It can be noticed that k^2 and k_e^2 are close for $k^2 << 1$

Value of k^2	2.00 %	15.00 %	25.00 %	50.00 %	60.00 %	81.00 %
Value of k_e^2	0.0204	0.1765	0.3333	1.0000	1.5000	4.2632

Figure 1 represents the relative frequency tuning range δf_{rel} as function of the coupling coefficient k_e^2 from equation (2). δf_{rel} is an increasing function with k_e^2. It is therefore necessary to maximize the coupling coefficient to increase the frequency tuning capability of piezoelectric VEHs. Moreover, by analyzing equation (2) and Figure 1, we notice that δf_{rel} is approximatively equivalent to $k_e^2/2$ when $k_e^2 << 1$. This approach allows to dimension very simply the limit of δf_{rel} of a linear VEH, which can be very useful for system designers.

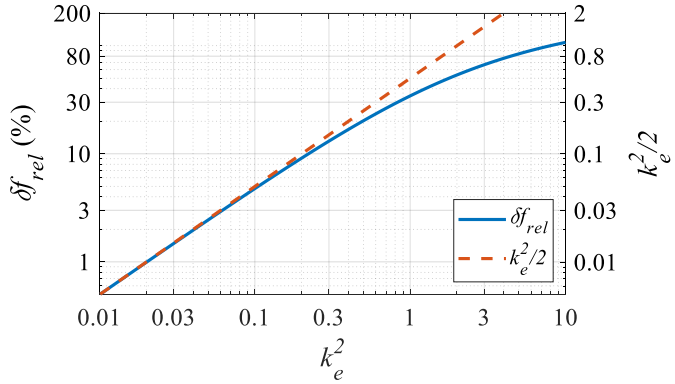

Figure 1: Relative frequency tuning range δf_{rel} as a function of the coupling coefficient

The two next sections consider the presentation of the studied device and the maximization its electromechanical coupling coefficient.

2.2. Device configuration

The studied VEH is a piezoelectric bimorph with a long proof mass (Figure 2) , as this design has been proven to be relevant for maximizing the global electromechanical coupling coefficient [8]. The long proof mass allows to homogenize the longitudinal distribution of strains in the beam and thus to increase the global electromechanical coupling coefficient k^2. The two piezoelectric layers and the substrate have the same length (L_b) and the same width (B). As it has been shown as optimal configuration [8], the piezoelectric layers are entirely covered with electrodes and their thickness are noted h_p (Figure 2.b). The proof mass is modeled by an equivalent point mass. The latter is described by a mass M_t and a rotational inertia I_t placed at a distance D_t from the free end of the beam on the neutral axis. Since the beams studied in this work are narrow (i.e. $L_b > 3B$), the assumption of plane stress is considered.

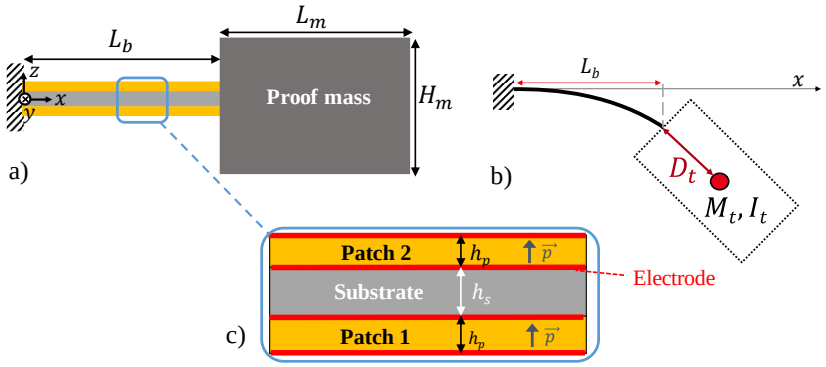

Figure 2: a) Cantilever with proof mass b) beam during bending c) beam layers and electrode connection.

2.3. Expression and maximization of the coupling coefficient k_e^2

Neglecting the beam mass compared to the proof mass and using a fully analytical model based on the Rayleigh method [8], the electromechanical coupling of the first bending mode of a piezoelectric bimorph with proof mass can be expressed thanks to equation (4). In the same manner as k_e^2 for k^2, k_{e31}^2 is a coefficient named expedient coupling coefficient of the piezoelectric material according to the 31-mode as expressed in (5).

$$k_e^2 = k_{e_{31}}^2 \mathcal{R}_L \mathcal{R}_T \tag{4}$$

$$k_{e31}^2 = \frac{k_{31}^2}{1 - k_{31}^2} \tag{5}$$

$\mathcal{R}_L$ and $\mathcal{R}_T$ are length and thickness factors respectively. $\mathcal{R}_T$ is related to the stress distribution in the thickness of the beam and is expressed by (6) . Y_s is the equivalent Young modulus of the substrate considered in plane stress, c_{11} is the linear elastic coefficient of the piezoelectric material according to the plane stress assumption. As discussed in the appendix, $\mathcal{R}_L$ only depends on the strain distribution along the beam and does not depend on the same parameter as $\mathcal{R}_T$.

$$\mathcal{R}_T = \frac{\left(\frac{h_p}{h_s}\right)^3 + 2\left(\frac{h_p}{h_s}\right)^2 + \left(\frac{h_p}{h_s}\right)}{\frac{1}{6}\left(\frac{Y_s}{c_{11}}\right) + \frac{4 + k_{e_{31}}^2}{3}\left(\frac{h_p}{h_s}\right)^3 + 2\left(\frac{h_p}{h_s}\right)^2 + \left(\frac{h_p}{h_s}\right)} \tag{6}$$

$\mathcal{R}_L$ and $\mathcal{R}_T$ are both smaller than 1 and the aim of the optimization process is to make them as close to unity as possible. The process of theoretically optimizing the longitudinal stress distribution and the transverse stress distribution (i.e. optimizing $\mathcal{R}_L$ and $\mathcal{R}_T$) can be carried out independently as they do not rely on the same parameters. The present work focusses on the $\mathcal{R}_T$ optimization as it is the only factor that depends on the materials properties.

$\mathcal{R}_T$ as a function of the thickness ratio is represented in Figure 3 for 3 stiffness ratios Y_s/c_{11} (0.1, 1 and 10) and 2 material coupling coefficients k_{e31}^2 (0.18 and 4.26 coherent values for PZT and PZN-5.5PT [011] respectively). It is shown that the optimal thickness ratio which maximizes $\mathcal{R}_T$ depends on the substrate and piezoelectric

materials. This optimal ratio, noted $h_p/h_s\big|^{\text{opt}}_{k_e^2}$, is determined by calculating the zero of the derivative of the $\mathcal{R}_T$ expression and is given by equation (7). $h_p/h_s\big|^{\text{opt}}_{k_e^2}$ matches a trade-off between maximizing the elastic energy in the piezoelectric material and homogenizing the strain distribution in the thickness of the material. It depends only on a rigidity ratio κ that is defined in (8).

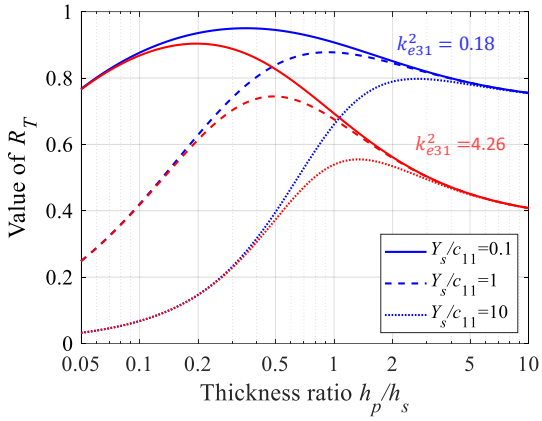

Figure 3: $\mathcal{R}_T$ as a function of the thickness ratio

$$\left.\frac{h_p}{h_s}\right|^{\text{opt}}_{k_e^2} = \begin{cases} \frac{1}{2}\kappa^{\frac{1}{3}}\left[\left(1-\sqrt{1-\kappa}\right)^{\frac{1}{3}}+\left(1+\sqrt{1-\kappa}\right)^{\frac{1}{3}}\right] & \text{for } \kappa \le 1 \\ \sqrt{\kappa}\cos\left(\frac{\arctan\sqrt{\kappa-1}}{3}\right) & \text{for } \kappa > 1 \end{cases} \tag{7}$$

$$\kappa = \frac{Y_s}{c_{11}}\frac{1}{k^2_{e_{31}}+1} \tag{8}$$

From Figure 3, we notice that the maximal value of $\mathcal{R}_T$ decreases with increasing $k^2_{e31}$and stiffness of the substrate. Furthermore, increasing k^2_{e31} increases the influence of the variation of the thickness ratio on the value of $\mathcal{R}_T$. Indeed, variation $\mathcal{R}_T$ function of h_p/h_s is more pronounced for $k^2_{e31} = 4.26$ than when $k^2_{e31} = 0.18$

The maximum value of $\mathcal{R}_T$ for piezoelectric and substrate materials combination, noted $\mathcal{R}_T^{max}$, is obtained by replacing h_p/h_s in (6) by $h_p/h_s\big|^{\text{opt}}_{k_e^2}$ from (7). Figure 4 shows $\mathcal{R}_T^{max}$ as a function of the Y_s/c_{11} ratio for three values of material expedient coupling coefficient k^2_{e31} (0.18, 0.33 and 4.26). From this figure, we notice that the stronger the coupling coefficient of the material, the more the value of the ratio c_{11}/Y_s impacts the value of $\mathcal{R}_T$ and, by extension, the achievable alternative coupling coefficient k_e^2.

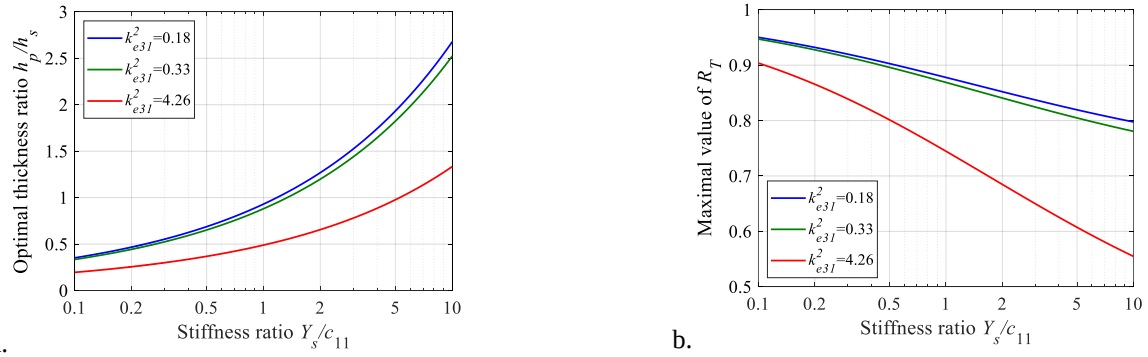

a. b.

Figure 4: a. Values of the optimal thickness ratio $h_p/h_s\big|^{\text{opt}}_{k_e^2}$ that maximize the coupling coefficient and b. the maximal value of $\mathcal{R}_T$ as a function of the stiffness ratio Y_s/c_{11}

From this discussion, it seems challenging to make piezoelectric cantilevers having an alternative coupling coefficient k_e^2 approaching the expedient coupling of the piezoelectric material k^2_{e31} with very strongly coupled materials. Moreover, Figure 4 reveals that the minimization of rigidity ratio κ through the choice of materials is of paramount importance in the optimization of piezoelectric beams.

2.4. Expression and maximization of the quality factor Q_m

We shew in the previous section the importance of increasing the electromechanical coupling coefficient to maximize the frequency bandwidth. Furthermore, considering the design of piezoelectric VEHs, their mechanical quality factors Q_m has also to be maximized in order to maximize the harvested power. Indeed, as expressed in (9), the maximal extracted power P_{max} is proportional to Q_m when $k_e^2 Q_m$ is sufficiently large (as an example : when $k_e^2 Q_m > 2$ for a resistive load [8]).

$$P_{max} = \frac{B_f^2}{M} \frac{Q_m}{8\omega_1} |\ddot{w}_b|^2 \tag{9}$$

Neglecting losses at the interfaces and considering that the air damping is negligible compared to the material losses for mesoscale VEHs, the overall losses of a VEH are dependents on the structural losses of the materials. The structural losses of the cantilever are therefore calculated considering the material losses of both substrate and piezoelectric material in this section.

Around a resonance frequency, the global structural losses can be expressed thanks to an imaginary part in the stiffness coefficient [18] as given in (10) where η is the mechanical loss factor of the cantilever. j is the imaginary unit.

$$K^* = K(1 + j\eta) \tag{10}$$

Around a resonance the loss factor can be related to a quality factor. While a loss factor induces a different behavior than a viscous damping away from the resonance, at the sort-circuit, using quality factors is a relevant figure of merit to compare systems and materials. We consider therefore the equivalent mechanical quality factor at resonance in this work to discuss the material performances.

Neglecting piezoelectric and dielectric losses in the cantilever at the short-circuit operation, η is equal to the inverse of the mechanical quality factor at the short-circuit resonance as expressed in (11) [19].

$$Q_m = \frac{1}{\eta} \tag{11}$$

The structural losses of the materials can identically be considered by imaginary parts on the materials coefficient as expressed in (12) and (13). Q_s is the substrate quality factor at the resonance and Q_p is the quality factor of the piezoelectric material at the short-circuit resonance.

$$Y_s^* = Y_s \left(1 + j\frac{1}{Q_s}\right) \tag{12}$$

$$c_{11}^* = c_{11} \left(1 + j\frac{1}{Q_p}\right) \tag{13}$$

By extending the model from [8], the stiffness is given in (14) with $(YI)^*$ the complex bending stiffness expressed in (15). a and b are expressed in appendix and depends on the beam length L_b and on the rotary inertia I_t and the mass M_t of the proof mass.

$$K^* = \frac{L_b(2\,a^2 + 6ab + 6\,b^2)}{6} YI^* \tag{14}$$

$$(YI)^* = B\left[Y_s^* \frac{h_s^3}{12} + \mathrm{c}_{11}^* \left(\frac{2}{3}\left(h_p + \frac{h_s}{2}\right)^3 - \frac{h_s^3}{12} + k_{e_{31}}^2 \frac{h_p^3}{6}\right)\right] \tag{15}$$

As only structural losses are considered, I_t, M_t and L_b are considered real and only $(YI)^*$ is complex in the expression of K^*. The quality factor of the cantilever is then calculated as the ratio of the real part and imaginary parts of K^* and therefore of $(YI)^*$ as expressed in (16). Q_m is finally expressed by (17).

$$Q_m = \frac{\mathrm{Real}[K^*]}{\mathrm{Imag}[K^*]} = \frac{\mathrm{Real}[(YI)^*]}{\mathrm{Imag}[(YI)^*]} \tag{16}$$

$$Q_m = Q_p \frac{\frac{1}{6}\frac{Y_s}{c_{11}} + \frac{4+k_{e31}^2}{3}\left(\frac{h_p}{h_s}\right)^3 + 2\left(\frac{h_p}{h_s}\right)^2 + \left(\frac{h_p}{h_s}\right)}{\frac{1}{6}\frac{Q_p}{Q_s}\frac{Y_s}{c_{11}} + \frac{4+k_{e31}^2}{3}\left(\frac{h_p}{h_s}\right)^3 + 2\left(\frac{h_p}{h_s}\right)^2 + \left(\frac{h_p}{h_s}\right)} \quad (17)$$

In this expression, the influence of dielectric and piezoelectric losses in the piezoelectric material on the short-circuit quality factor is neglected.

Figure 5 and Figure 6 represent the expected overall short-circuit quality factor Q_m as a function of h_p/h_s for $Y_s/c_{11} \in \{0.1; 1; 10\}$ and $k_{e31}^2 = 0.18$ and $k_{e31}^2 = 4.26$ respectively. For both figures, Q_p=100 and $Q_s \in \{250\,; 500\}$. From these figures, we notice that a high substrate quality factor Q_s leads to an interesting positive impact on Q_m (i.e. $Q_m > Q_p$) when the substrate is thick. However, the value h_p/h_s for which Q_s has a significant impact on Q_m is usually distant from the optimal thickness ratio $h_p/h_s\big|_{k_e^2}^{\text{opt}}$ defined in (7). As an illustration, the values of $h_p/h_s\big|_{k_e^2}^{\text{opt}}$ are represented in Figure 5 and Figure 6. At $h_p/h_s\big|_{k_e^2}^{\text{opt}}$, Q_m does not reach higher values than 103 and 111 for $k_{e31}^2 = 0.18$ and $k_{e31}^2 = 4.26$ respectively. Moreover, it is interesting to notice that increasing the material coupling k_{31}^2 does not affect much the overall Q_m as the trends are similar in Figure 5 and Figure 6. Only the optimal thickness ratios $h_p/h_s\big|_{k_e^2}^{\text{opt}}$ are affected, which slightly alters Q_m at the optimal thickness ratio.

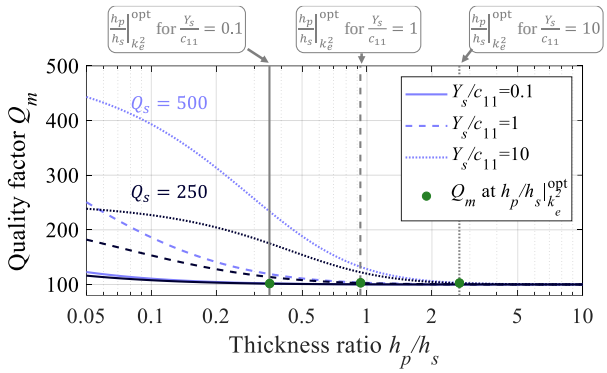

Figure 5: Theoretical quality factor Q_m as a function of the thickness ratio for $Q_p = 100$, $k_{e31}^2 = 0.18$, $Y_s/c_{11} \in \{0.1; 1; 10\}$ and $Q_s \in \{250; 500\}$

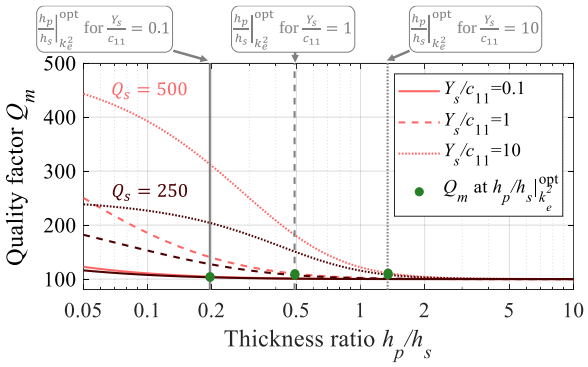

Figure 6: Theoretical quality factor Q_m as a function of the thickness ratio for $Q_p = 100$, $k_{e31}^2 = 4.26$, $Y_s/c_{11} \in \{0.1; 1; 10\}$ and $Q_s \in \{250; 500\}$

Nevertheless, a non-negligible negative impact of Q_s on Q_m can be observed when $Q_s < Q_p$. Figure 7 and Figure 8 represent Q_m as a function of h_p/h_s when $Q_s = 20$ (i.e. $Q_p/5$). At $h_p/h_s\big|_{k_e^2}^{\text{opt}}$, Q_m is between 87 and 91 for $k_{e31}^2 = 0.18$ and it is between 61 and 82 for $k_{e31}^2 = 4.26$. As, in comparison, $Q_m \leq 111$ for $Q_s = 5 \times Q_p$, the influence of Q_s on Q_m appears more pronounced when $Q_s < Q_p$ than when $Q_s > Q_p$.

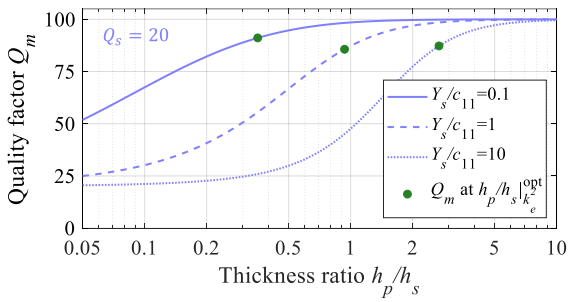

Figure 7: Theoretical quality factor Q_m as a function of the thickness ratio for $Q_p = 100$, $k_{e31}^2 = 0.18$, $Y_s/c_{11} \in \{0.1; 1; 10\}$ and $Q_s = 20$

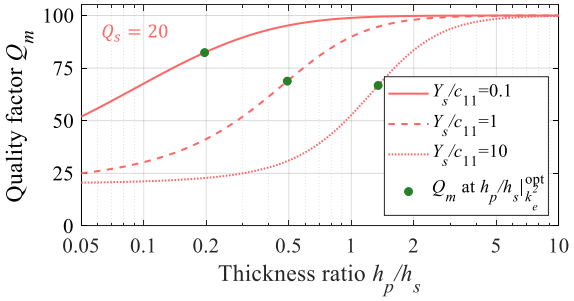

Figure 8: Theoretical quality factor Q_m as a function of the thickness ratio for $Q_p = 100$, $k_{e31}^2 = 4.26$, $Y_s/c_{11} \in \{0.1; 1; 10\}$ and $Q_s = 20$

In conclusion of this section, a lowly damped substrate material does not impact much on overall short-circuit quality factor Q_m when the thickness ratio is chosen to maximize the electromechanical coupling coefficient. In contrast, using a high-loss substrate material can drastically hinder the overall quality factor.

As k_e^2 and Q_m are both relevant considering the energy harvesting performance of a piezoelectric cantilever, both have to be maximized simultaneously. However, there is a compromise in the thickness optimization. Indeed, maximizing k_e^2 leads to an optimal thickness ratio $h_p/h_s\big|_{k_e^2}^{\text{opt}}$ while maximizing Q_m leads to: either the lowest h_p/h_s possible when $Q_s > Q_p$, either to the highest h_p/h_s possible when $Q_s < Q_p$. As a solution, we propose to maximize the product $k_e^2 Q_m$ to optimize the performance of our cantilever. $k_e^2 Q_m$ is a relevant figure of merit for piezoelectric devices as its maximization induces the maximization of the product of the maximal harvested power and the frequency bandwidth. $k_e^2 Q_m$ has already been considered in literature to compare VEHs [17,20,21], but no modelling was proposed for design purpose. The next section is dedicated to derivation of the expression of $k_e^2 Q_m$ and its maximization.

2.5. Expression and maximization of $k_e^2 Q_m$

$k_e^2 Q_m$ is expressed in (18) thanks to the expressions of ${k_e}^2$ and Q_m given in equations (4) and (17). $k_e^2 Q_m$ is the product of $k_{e31}^2 Q_p$ (describing the piezoelectric material performance), $\mathcal{R}_L$ and a factor $\mathcal{R}_Q$ expressed in (19).

$$k_e^2 Q_m = k_{e31}^2 Q_p \, \mathcal{R}_L \mathcal{R}_Q \tag{18}$$

$$\mathcal{R}_Q = \frac{\left(\frac{h_p}{h_s}\right)^3 + 2\left(\frac{h_p}{h_s}\right)^2 + \left(\frac{h_p}{h_s}\right)}{\frac{1}{6}\left(\frac{Q_p}{Q_s}\right)\left(\frac{Y_s}{c_{11}}\right) + \frac{4 + k_{e31}^2}{3}\left(\frac{h_p}{h_s}\right)^3 + \left(\frac{h_p}{h_s}\right)^2 + \left(\frac{h_p}{h_s}\right)} \tag{19}$$

It is interesting to notice that the influence of the substrate material properties on $\mathcal{R}_Q$ is defined by the ratio $\left(\frac{Q_p}{Q_s}\right)\left(\frac{Y_s}{c_{11}}\right)$ and that the ratio $\left(\frac{Y_s}{c_{11}}\right)$ does not appear alone any more compared to the expression of $\mathcal{R}_T$. Considering with $\mathcal{R}_L$=1, Figure 9 and Figure 10 represent the value of $k_e^2 Q_m$ as a function of h_p/h_s for k_{e31}^2 =0.18 and k_{e31}^2=4.26 respectively, when Q_p =100, $Y_s/c_{11} \in \{0.1; 10\}$ and $Q_s \in \{20; 500\}$. The values of $k_e^2 Q_m$ for $h_p/h_s\big|_{k_e^2}^{\text{opt}}$ (i.e. thickness ratios that maximize k_e^2 given in (7)) are marked with green dots in the figures.

In Figure 9 and Figure 10, the value of $k_e^2 Q_m$ is maximal for an optimal thickness ratio. This optimal thickness ratio, denoted $h_p/h_s\big|_{k_e^2 Q_m}^{\text{opt}}$, differs from $h_p/h_s\big|_{k_e^2}^{\text{opt}}$. $h_p/h_s\big|_{k_e^2 Q_m}^{\text{opt}}$ is greater than $h_p/h_s\big|_{k_e^2}^{\text{opt}}$ when $Q_s < Q_p$and $h_p/h_s\big|_{k_e^2 Q_m}^{\text{opt}}$ is lower than $h_p/h_s\big|_{k_e^2}^{\text{opt}}$ when $Q_s > Q_p$. Nevertheless, while $h_p/h_s\big|_{k_e^2}^{\text{opt}}$ can be twice as small or larger than $h_p/h_s\big|_{k_e^2 Q_m}^{\text{opt}}$, the value of $k_e^2 Q_m$ at $h_p/h_s\big|_{k_e^2}^{\text{opt}}$ is not much smaller than at $h_p/h_s\big|_{k_e^2 Q_m}^{\text{opt}}$(under 30% relative decrease in Figure 9 and Figure 10).

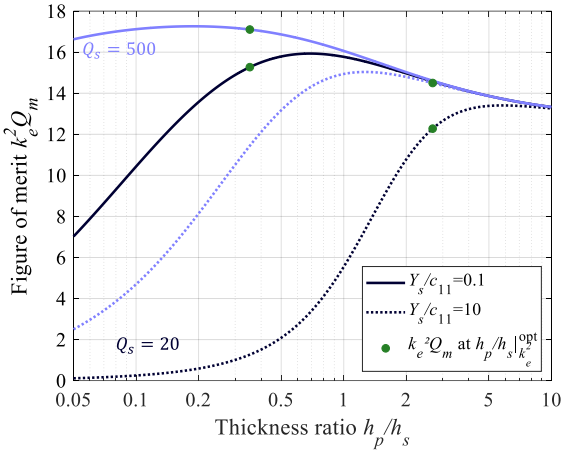

Figure 9: Theoretical value of $k_e^2 Q_m$ considering $\mathcal{R}_L = 1$, for $k_{e31}^2 = 0.18$, $Q_p = 100$ and $Q_s \in \{20; 500\}$. The values of $h_p/h_s\big|_{k_e^2}^{\text{opt}}$ are computed from (7).

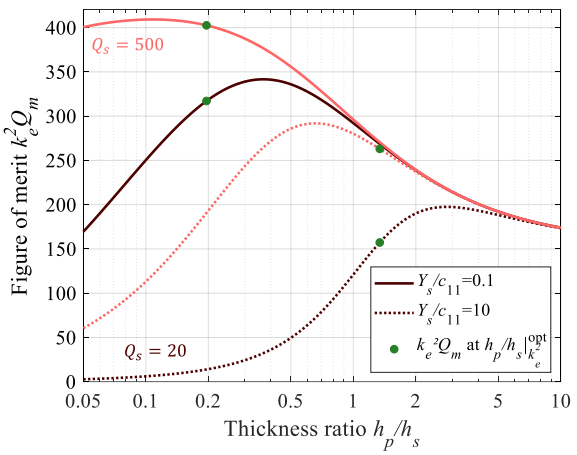

Figure 10: Theoretical value of $k_e^2 Q_m$ considering $\mathcal{R}_L = 1$, for $k_{31}^2 = 4.26$, $Q_p = 100$ and $Q_s \in \{20; 500\}$. The values of $h_p/h_s\big|_{k_e^2}^{\text{opt}}$ are computed from (7).

The optimal thickness ratio $h_p/h_s\big|^{\text{opt}}_{k_e^2 Q_m}$ maximizing $k_e^2 Q_m$ can be analytically expressed as a function of material properties Y_s, c_{11}, Q_p, Q_s and k_{31}^2. This optimal ratio is determined by calculating the zero of the derivative of $\mathcal{R}_Q$ in expression (19) and is given in (20). In the same way as $h_p/h_s\big|^{\text{opt}}_{k_e^2}$, $h_p/h_s\big|^{\text{opt}}_{k_e^2 Q_m}$ only depends on a new parameter κ_Q, expressed in (21).

$$\left.\frac{h_p}{h_s}\right|^{\text{opt}}_{k_e^2 Q_m} = \begin{cases} \frac{1}{2}\kappa_Q^{\frac{1}{3}}\left[\left(1-\sqrt{1-\kappa_Q}\right)^{\frac{1}{3}}+\left(1+\sqrt{1-\kappa_Q}\right)^{\frac{1}{3}}\right] & \text{for } \kappa_Q \le 1 \\ \sqrt{\kappa_Q}\cos\left(\frac{\arctan\sqrt{\kappa_Q-1}}{3}\right) & \text{for } \kappa_Q > 1 \end{cases} \tag{20}$$

$$\kappa_Q = \frac{Q_p}{Q_s}\frac{Y_s}{c_{11}}\frac{1}{k_{e_{31}}^2+1} \tag{21}$$

As a result, for a piezoelectric material (i.e. fixed values of k_{e31}^2, c_{11} and Q_p), $h_p/h_s\big|^{\text{opt}}_{k_e^2 Q_m}$ and the maximal achievable $k_e^2 Q_m$ only depend on the ratio Q_s/Y_s. Indeed, looking at equation (19), the same value of $k_e^2 Q_m$ is expected as long as Q_s/Y_s is held constant, regardless of the values of Q_s and Y_s. This reveals that the influence of the substrate material properties on $k_e^2 Q_m$ is defined by the ratio Q_s/Y_s.

$h_p/h_s\big|^{\text{opt}}_{k_e^2 Q_m}$ is represented as a function of $c_{11}/Y_s \times Q_s/Q_p$ in Figure 11. Replacing the value of $h_p/h_s\big|^{\text{opt}}_{k_e^2 Q_m}$ in the expression of $k_e^2 Q_m$ in (18) leads to the maximal achievable value of $k_e^2 Q_m$ for a combination of given piezoelectric and substrate materials. Figure 12 represents the ratio between the maximal achievable $k_e^2 Q_m$ and $k_{e31}^2 Q_p$ as a function of $c_{11}/Y_s \times Q_s/Q_p$.

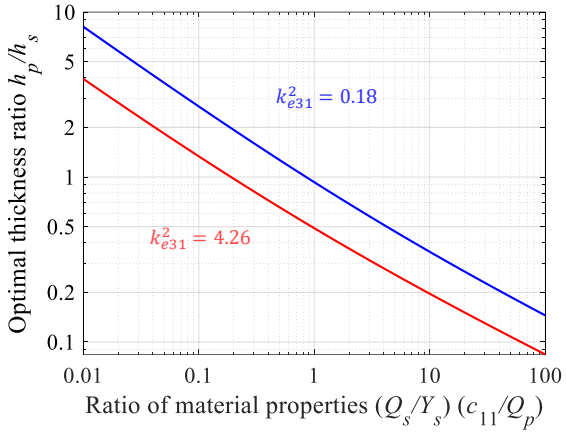

Figure 11: Values of the optimal thickness ratio $h_p/h_s\big|^{\text{opt}}_{k_e^2 Q_m}$ that maximize $k_e^2 Q_m$

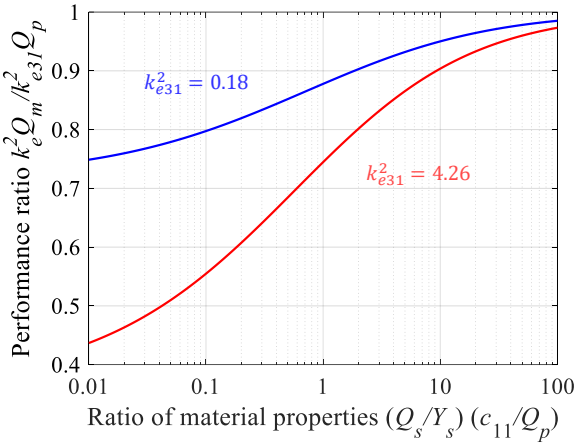

Figure 12: Maximal theoretical value of $k_e^2 Q_m/k_{e31}^2 Q_p$ (i.e. maximal value of $\mathcal{R}_Q$) as a function of the ratio of the material properties $\left(\frac{Q_p}{Q_s}\right)$ $\left(\frac{Y_s}{c_{11}}\right)$

Figure 12 shows that the achievable value of $k_m^2 Q_m$ increases when Q_s/Y_s increases. A substrate material with a high-quality factor and low Young modulus has to be chosen in order to maximize $k_e^2 Q_m$. This appears challenging as low damped metal are usually stiff and soft polymers are usually lossy. We can also notice that realizing a cantilever whose $k_e^2 Q_m$ approaches $k_{e31}^2 Q_p$ is more challenging with a strongly coupled material. Indeed, $k_e^2 Q_m/k_{e31}^2 Q_p$ is lower when k_{e31}^2 is equal to 4.36 than when it is equal to 0.18.

We furthermore observe that $k_e^2 Q_m$ is always lower than $k_{e31}^2 Q_p$. As a result, the expected performances of a bimorph cantilever in terms of $k_e^2 Q_m$ is always lower than $k_{e31}^2 Q_p$. It is important to note that this assertion is only proven here for bimorph with piezoelectric patches having the same surface as the substrate. We do not claim its truthfulness for unimorphs or bimorphs that are not completely covered with piezoelectric material. Nevertheless, bimorph structures are necessary to maximize the global coupling coefficient. As a conclusion, in the field of cantilevers dedicated to resonant frequency tuning, efforts must be made to get bimorphs for which $k_e^2 Q_m$ is as close as possible to $k_{e31}^2 Q_p$.

To conclude, this modelling section offers significant insight about the design of cantilever with high value of figure of merit $k_e^2 Q_m$. As it will be discussed in the following section with the design of strongly coupled VEH, the proposed model offers meaningful guidelines for the determinant choices. In particular, we can point out guidelines: soft substrate material allows maximizing k_e^2, a moderate increase of Q_s does not affect much Q_m for bimorphs when the thicknesses are optimized to maximize k_e^2, the Q_s/Y_s ratios of substrates have to be evaluated to maximize $k_e^2 Q_m$.

In the following section, we detail the design of a strongly coupled VEH and the experimental validation of its performance.

3. Design configuration

3.1. Design purpose

This section discusses the design process of a strongly coupled VEH having low mechanical losses. The aim of our work is to design and fabricate a VEH with small dimensions and a short-circuit resonant frequency of less than 200 Hz. The PZN-5.5PT [011] material has been chosen as piezoelectric material as we aim to get really strong global coupling coefficient k^2 for resonant frequency tuning by electrical methods. Indeed, PZN-5.5PT [011] is one of the most coupled piezoelectric material regarding transverse coupling modes (k_{32}^2=81%, $k_{e32}^2 = 4.26$).

Metals (brass, steel and aluminum) were considered for the substrate materials as they have the advantage of having high quality factors and being easily machined by mechanical parts suppliers. The proof mass is made of steel thanks to its availability and its high density ($\rho_{steel} = 7930\ \mathrm{kg/m^3}$). Each substrate material (brass, steel and aluminum) was considered to provide a prototype configuration. The expected $k_e^2 Q_m$ for each material substrates are discussed.

In addition to the material coefficients, the design of our VEH is guided by its manufacturing configuration which leads to strategic dimensioning choices. Indeed, due to the configuration of the prototype, spacings are required between the patches and the stationary frame at one end and between the patches and the proof mass at the opposite end (Figure 13). These spacings are noted d_c and d_m in Figure 13. Although these distances and the thickness of the adhesive between the patches and the substrate cannot be determined precisely and are as restrained as possible, they induce a drastic decrease in k^2.

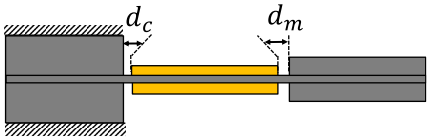

Figure 13: Representation of the functional spacings

As the material losses are hardly available *a priori*, the VEH design has been realized as follow. A preliminary design is realized to maximize k_e^2 for each of the 3 metallic substrates. The influence of the spacings is then analyzed by mean of a 3D finite element simulation software. Finally, the material losses are measured from bare beams and piezoelectric materials separately and their influence on the global cantilever are computed and compared.

3.2. Preliminary design

A preliminary design has firstly established by the used of the model (equation (4)) to maximize k_e^2. The length of the beam L_b and the proof mass shape have been optimized to maximize the $\mathcal{R}_L$ factor and to adjust the resonant frequency in a restrained volume. The thicknesses have been considered to maximize $\mathcal{R}_T$ and regarding the production constraints of the suppliers. The substrate thicknesses h_s have furthermore been taken a bit bigger than the corresponding optimal ratio $h_p/h_s\big|_{k_e^2}^{\mathrm{opt}}$ in order to limit the influence of the spacing d_c and d_m (Figure 13) which is discussed in the next section. The shared geometric parameters established for the three substrate materials are shown in Table 2. The selected thicknesses for each metal are provided in Table 3.

Table 2: Geometrical parameters considered for the design

Beam length L_b	15 mm
Proof mass length L_m	20 mm
Proof mass height H_m	4 mm
Patches thickness h_p	0.4 mm
Beam and proof mass width B	5 mm

The expected coupling coefficients and short-circuit resonant frequency are given from the proposed model in Table 3 and are compared to 2D FEM simulation and 3D FEM simulation.

Table 3: Material Young modulus, selected thickness and expected coupling coefficients

Material	Y_s	h_s	Model		2D -FEM		3D FEM	
			f_{sc}	k_e^2	f_{sc}	k_e^2	f_{sc}	k_e^2
Aluminum	69 GPa	0.5 mm	130.5 Hz	2.07	131.3 Hz	1.84	142.9 Hz	1.71
Brass	110 GPa	0.4 mm	119.2 Hz	1.97	119.9 Hz	1.74	125.1 Hz	1.62
Steel	200 GPa	0.3 mm	107.7 Hz	1.84	108.3 Hz	1.65	113.1 Hz	1.53

From Table 3, we notice that the model is close to FEM simulations in the determination of the short-circuit resonant frequency. The differences regarding the coupling coefficient between the 2D-FEM and 3D-FEM is due to the not full respect of plane stress assumption ($L_b/B < 10$). The three design propositions offer close resonant frequencies. As aluminum is softer than brass and steel, the optimal thickness h_s is greater for aluminim than for brass and steel. Aluminum also offers the best value of expected coupling coefficient.

3.3. Spacing influences

.

The influence of the spacings have then been observed for the three configurations. The expected coupling coefficients of the VEHs were calculated thanks to 3D modal analyses on Comsol Multiphysics (Figure 14) in short-circuit and open-circuit conditions. These calculations were conducted considering equal values of d_c and d_m from 50 µm to 300µm. Figure 15 shows the expected coupling as function of the size of the spacings.

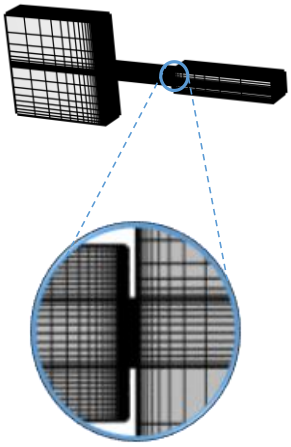

Figure 14: Meshing on Comsol Multiphysics for the functional clearance

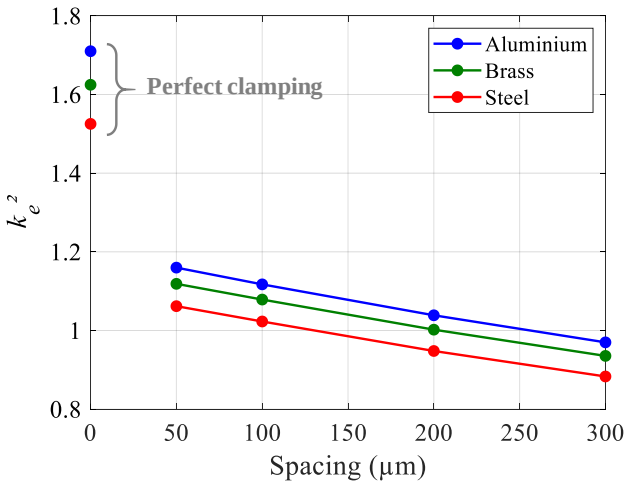

Figure 15: Expected expedient coupling coefficient k_e^2 from 3D-FEM simulations for equals spacings d_c and d_m

According to Figure 15, the spacings induce a drastic decrease of the expedient coupling coefficient k_e^2. The diminution of k_e^2 increases with the increase of d_c and d_m as the spacing is increasingly flexible. Indeed, the diminution of k_e^2 is due to the increasing elastic energy that is stored in the substrate material at the spacings rather than in the piezoelectric material. Increasing the thickness h_s of the substrate can reduce the impact of the spacings. Nevertheless, increasing too much h_s will eventually have a negative impact on the coupling coefficient. The aluminum configuration offers the best coupling coefficient even when the spacings are considered. For d_c and d_m equaling 300 µm, k^2 is equal to 0.97, 0.93 and 0.88 for the aluminum, brass and steel respectively. The next section considers the estimation of the quality factor before proceeding to the final design by the analysis of $k_e^2 Q_m$.

3.4. Quality factor and final design

.

The PZN-PT patches were cut at size by the manufacturer Microfine. Based on the supplier datasheet [22], the quality factor Q_p at the short-circuit resonant frequency of PZN-5.5PT [011] is between 80 and 170 for the 32-mode. This variation is due to nonlinear mechanical losses which increase together with the excitation level. The quality factor of the patches has finally been measured at 247 in our laboratory using an impedance analyzer at 0.1 V amplitude. The difference with the datasheet is explained with the very low excitation level.

The substrates beams have been purchased for the 3 metals in order to determine their quality factor Q_s under sinusoidal vibration excitation (0.5 m/s² acceleration amplitude). Neglecting the air damping losses, the quality factor of the substrates can be considered equal to the measured quality factor of the beams. Q_m is finally calculated from the values of Q_p and Q_s using equations (17) and is given in

Table 4. $k_e^2 Q_m$ is given taking the value of k_e^2 obtained using the proposed model (in Table 3) and for spacings d_c and d_m equal to 300 µm from 3D FEM.

Table 4: Measured substrate quality factors Q_s and expected VEH performances obtained using the proposed model (perfect clamping) and using 3D FEM ($d_c = d_m = 300$ µm)

Material	Q_s	Q_s/Y_s (GPa^{-1})	k_e^2 model	k_e^2 spacings	$Q_p = 80$			$Q_p = 247$		
					Q_m	$k_e^2 Q_m$ model	$k_e^2 Q_m$ spacings	Q_m	$k_e^2 Q_m$ model	$k_e^2 Q_m$ spacings
Aluminum $h_s = 0.5$ mm	273	**3.96**	**2.07**	**0.97**	103	**212.97**	**99.5**	255	528	246.9
Brass $h_s = 0.4$ mm	430	3.91	1.97	0.93	106	208.78	**99.5**	284	**557**	**265.4**
Steel $h_s = 0.3$ mm	**605**	3.03	1.84	0.88	106	196.11	94.0	**297**	548	262.6

Although aluminum emerges as the best candidate to maximize $k_e^2 Q_m$, the three metals offer almost the same value of Q_s/Y_s. All the substrates allow to get very strong $k_e^2 Q_m$. This is possible thanks to the outstanding performances of the PZN-PT ($341 < k_{e31}^2 Q_p < 1\,053$ depending on the value of Q_p) and the design optimization. We notice a strong influence of the spacings on the value of $k_e^2 Q_m$ due to the decrease of the expedient coupling coefficient k_e^2. $k_e^2 Q_m$ is divided by around 2 between the perfect clamping configurations from the model and the configurations with spacings of 300 µm from the 3D FEM.

While aluminum offers the best performances for $Q_p = 80$, it is the worst at $Q_p = 247$ as the substrate thickness is not taken to optimal ratio $h_p/h_s\big|^{\text{opt}}_{k_e^2 Q_m}$. Indeed, the substrates thicknesses that is optimal depend on the value of Q_p. While the $k_e^2 Q_m$ performances are almost similar considering the spacings between the three substrate configurations, aluminum substrate has been chosen for two reasons: it offers the best performances for Q_p equal to 80 that corresponds to relatively "high" acceleration level, and it reduces stress jump at the substrate / piezoelectric interface compared to brass and steel as its Young modulus is the closest to the PZN-5.5PT one.

4. Measurements and results

4.1. Fabrication and identification

The piezoelectric patches were bonded with epoxy glue in our laboratory to the aluminum beam. The proof mass was also bonded to the substrates with an epoxy glue. Figure 16 depicts the final prototype.

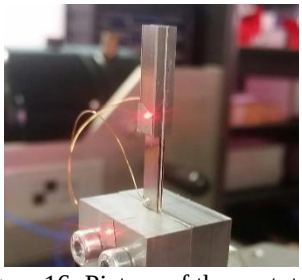

Figure 16: Picture of the prototype

The power output of the prototype was determined under sinusoidal vibration excitation (Figure 17). The vibrations were generated and controlled by an electromagnetic vibrator (K2075E-HT) driven by a DSpace board and the acceleration level was monitored using an accelerometer (Piezotronics 356A17 PCB). The DSpace board was controlled by a dedicated Matlab script that defined the level, the acceleration frequency and controlled the programmable electrical resistance. Experiments were performed for 10 resistive loads between 800 Ω and 25 MΩ over 400 excitation frequencies between 105 Hz and 155 Hz. The displacement was measured on the proof mass 4 mm from the beam end (i.e. at $x = L_b + 4$ mm) thanks to a laser vibrometer as shown in Figure 17.

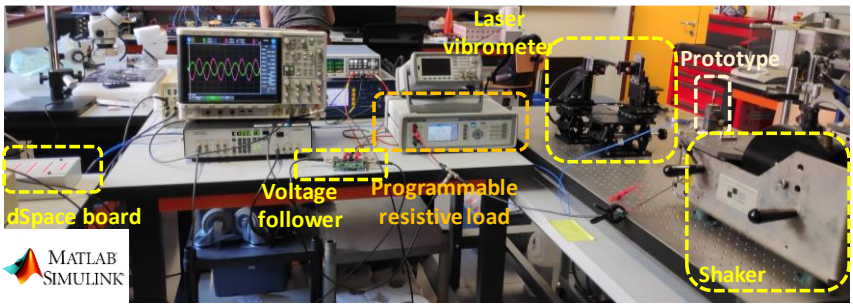

Figure 17: Experimental test bench

The mean harvested power is represented for few resistances in Figure 18. As the prototype exhibits a softening behavior and nonlinear losses with the variation of the acceleration level, the measurements have been fitted with the one mechanical degree of freedom nonlinear model presented in [23]. The fitted coefficients of the equations of movement and current given in (22) and (23) are summarized in Table 5. In (22) and (23), r, v and w_b are the relative displacement of the proof mass, the voltage across the electrodes and the displacement of the base (i.e. clamped end) .

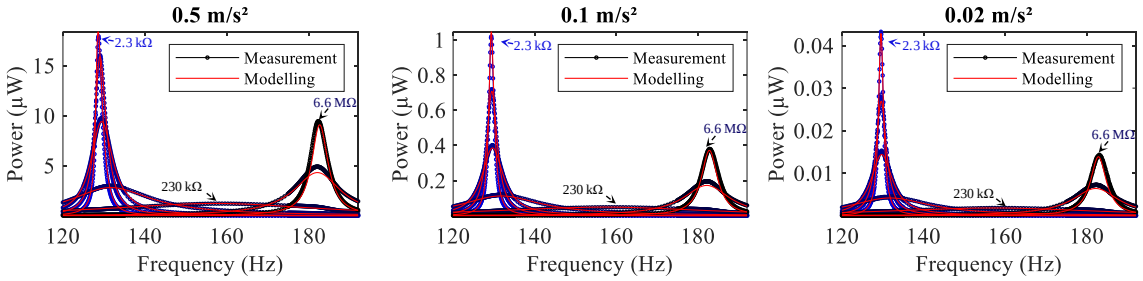

Figure 18: Experimental extracted power at 0.5 m/s² (left), 0.1 m/s² (center) and 0.02 m/s² (right) accelerations, for several resistive loads: 2.3 kΩ, 6.2 kΩ, 14.3 kΩ , 57.8 kΩ, 230 kΩ, 1.67 MΩ and 6.6 MΩ.

$$M\ddot{r} + Kr + K_2 r^2 \mathrm{sgn}(r) - \Theta v - \Theta_2 v r \mathrm{sgn}(r) + (b_1 r \mathrm{sgn}(r) + b_2 r^2)\mathrm{sgn}(\dot{r}) = -B_f \ddot{w}_B \quad (22)$$

$$\Theta \dot{r} + \Theta_2 r \dot{r} \mathrm{sgn}(r) + C_p \dot{v} + \frac{v}{R_{load}} + \left(d_1 \dot{v} \mathrm{sgn}(v)\right)\mathrm{sgn}(\dot{v}) = 0 \quad (23)$$

Table 5: Coefficients deduced from the experiments.

Name	Coefficient	Value
Equivalent mass	M	7.1 g
Forcing term	B_f	4.9 g
Linear stiffness	K	4 729 N/m
Coupling term	Θ	-4.26×10^{-3} N/V
Capacitance	C_p	3.88×10^{-9} F
Nonlinear stiffness	K_2	-2.34×10^{6} N/m²
Nonlinear coupling term	Θ_2	5.07×10^{-3} N/Vm
Linear mechanical loss	b_1	29.57 N/m
Nonlinear mechanical loss	b_2	9.15×10^{5} N/m²
Linear dielectric loss	d_1	5.29×10^{-11} F

We notice that the results deduced from the model are close to the measurements despite the wide frequency range of measurements. The model therefore allows to describe the performances of the fabricated VEH in the next sections.

As the nonlinear mechanical loss coefficient b_2 is non-null in Table 5, the prototype exhibits increasing mechanical losses with the increase of the acceleration amplitude level. While the harvested mean power is weak at 0.02 m/s² (lower than 0.05 µW), the mean power reaches almost 18 µW at 0.5 m/s² around the power peak corresponding to the short-circuit resonant frequency.

4.2. $k_e^2 Q_m$ performances analysis

Two power peaks are present in Figure 18 as the prototype exhibits a strong coupling coefficient and a high quality factor. By considering the considering the linear behavior of the harvester at low excitation level, the global coupling coefficient k^2 is estimated from the linear coefficients Θ, K and C_p from equations (22) and (23) using equation (24). k^2 is therefore equal to 49.8 % (i.e. $k_e^2 = k^2/(1-k^2) = 0.99$). This experimental value is close to the value (0.97) predicted by the 3D-FEM simulations considering spacings of 300 µm in

Table 4.

$$k^2 = \frac{\Theta^2}{\Theta^2 + KC_p} \tag{24}$$

The quality factor in short circuit condition can also be estimated using the linear coefficients K and b_1. Indeed, the structural losses coefficient b_1 can be expressed as a function of the imaginary part of the complex stiffness K [24] and then, using (10), as a function of the quality factor in short-circuit condition as express in (25).

$$b_1 = \frac{\pi}{2}\mathrm{Imag}(K^*) = \frac{\pi}{2}\frac{K}{Q_m} \tag{25}$$

$$Q_m = \frac{\pi K}{2b_1} \tag{26}$$

Using equation (26), Q_m is estimated at 251 from the linear coefficients K and b_1. As the losses increases with the acceleration level, the quality factor in short-circuit condition can be determined for different given acceleration amplitudes. Taking b_2 null and fitting the power by changing b_1 allows to determine the equivalent linear loss factor at a given acceleration level. By this way, we determine that Q_m is equal to 236 at 0.02 m/s² and to 142 at 0.5 m/s². These values of Q_m are within the range of those expected by the model in

Table 4.

As a result, the figure of merit $k_e^2 Q_m$ is equal to 140.9 at 0.5 m/s². This result has been made possible by choosing the appropriate material and by limiting the strain amplitude in the piezoelectric material (to avoid strong nonlinear losses).

4.3. Experiments on a tunable electrical interface

The VEH has been tested with an electrical interface able to tune the resonant frequency: the SC-SECE [3]. The SC-SECE strategy allows to adjust the shape of the voltage waveform in order to tune the electrically-induced force on the VEH (due to the indirect piezoelectric effect) and therefore its resonant frequency. A system-level implementation of the SC-SECE strategy is shown in Figure 19.a. During a semi-period of vibration, the SC-SECE strategy operates sequentially in three different working phases: open-circuit, resonant energy collection, and short-circuit.

The SC-SECE includes two electrical tuning parameters, ϕ_S and $\Delta\phi$, which allow to control the durations of the short-circuit and open-circuit phases respectively. An example of piezoelectric voltage waveform obtained with the SC-SECE and given values of ϕ_s and $\Delta\phi$ is shown in Figure 19.b. As described extensively in [3], the values of ϕ_S and $\Delta\phi$ have an impact on an electrically-induced damping and an electrically-induced stiffness that allow to electrically-tune the VEH dynamics. The extracted power with the combination of the proposed prototype and the SC-SECE circuit has been measured for sinusoidal vibrations characterized by a 0.34 m/s² acceleration amplitude, with 75 vibration frequencies (chosen between 110 Hz and 220 Hz) and 40 values of ϕ_s and $\Delta\phi$ (chosen between 0° and 180°), for a total of 120000 acquisitions. For each vibration frequency, the optimal combination of ϕ_s and $\Delta\phi$ maximizing the extracted power and the value of the extracted power are shown in Figure 20. The

expected theoretical power and optimal ϕ_s and $\Delta\phi$, considering the SC-SECE theory [3] with a quality factor of 181, are also illustrated in Figure 20.

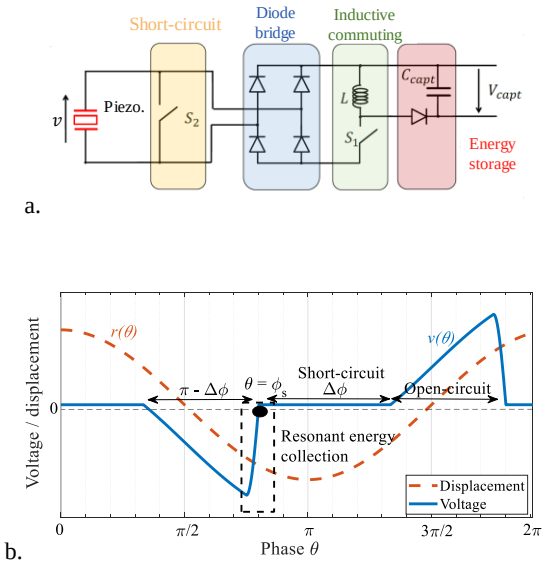

Figure 19: a. circuit implementing the SC-SECE technique, b. voltage and displacement waveforms

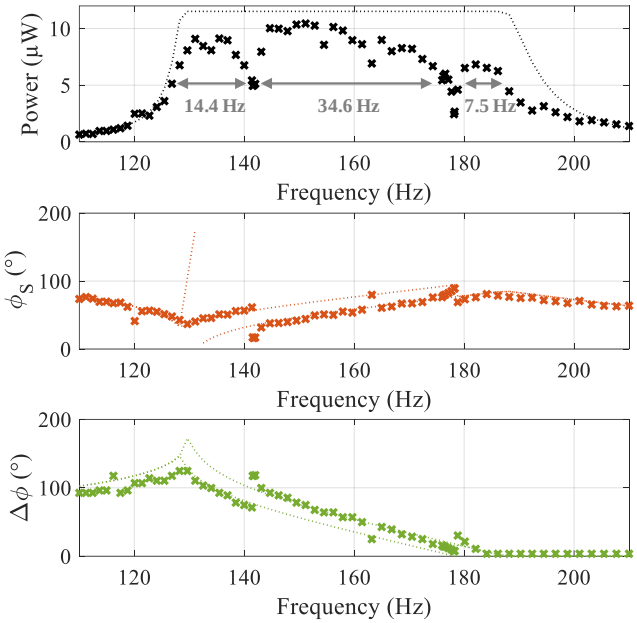

Figure 20: Extracted power with the SC-SECE for optimal values of ϕ_s and $\Delta\phi$

The measured extracted power with the SC-SECE technique reaches a maximum at 10.4 µW. With SC-SECE, the extracted power should theoretically remain constant between the short-circuit and open-circuit resonant frequency. A decrease of experimental power with the increasing frequency is however observed and is due to the dielectric losses expressed by d_1 in equation (23). Moreover, power drops can be observed around 142 Hz and 178 Hz. At these frequencies, the power is equal to 5.0 µW and 2.7 µW respectively. While these drops hinder the frequency tuning ability as they go below the half of the maximal power ($P^{max} = 10.44$ µW), they offer an interesting insight to understand the behavior of strongly coupled VEHs. The origin of these drops seems to be due to the interaction of the second bending mode of vibration, which is not considered with the single degree of freedom model in (22). Indeed, high-frequency oscillations of the voltage can be noticed at almost the same frequency as the second mode (Figure 21 and Figure 22). These figures represent the voltage waveforms at 130.0 Hz and 141.7 Hz on which harmonic components whose frequencies are around 1600 Hz are observed. As a comparison the second bending mode has its short-circuit resonant frequency at 1513 Hz and open circuit resonant frequency at 1 622 Hz (the coupling coefficient k^2 of the second bending mode is equal to 14 %). Nevertheless, despite the neglect of the second mode of vibration, the predictions of the model are relatively good for the experiments with the SC-SECE technique (Figure 20)

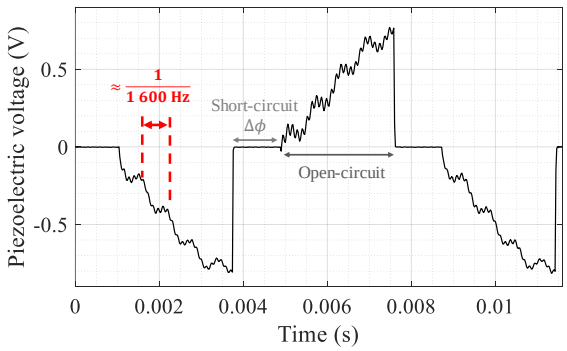

Figure 21: Voltage waveform with the SC-SECE at 130.0 Hz for $\phi_s = 84\,°$ and $\Delta\phi = 53\,°$

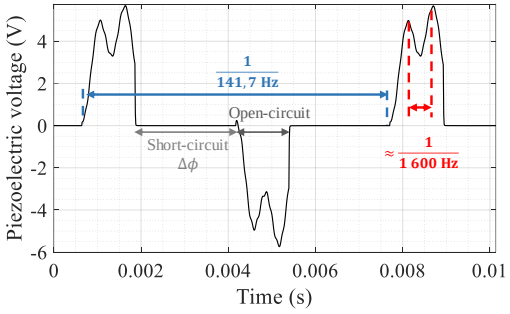

Figure 22: Voltage waveform with the SC-SECE at 141.7 Hz for optimal ϕ_s (=16.2°) and $\Delta\phi$ (=117.5°)

Thanks to the SC-SECE technique (Figure 20), the frequency range for which the power extracted is at least half of the maximum power is equal to 56.5 Hz (i.e. 36.0 % of the central frequency). Furthermore, the proposed VEH offers sufficient power to supply a wireless sensor node (10 µW at 0.34 m/s²) in a small overall volume. The normalized power density (NPD) given by NPD=Power/(Overall Volume×Acceleration²) is calculated and compared to strongly coupled VEHs associated with electrical resonant frequency tuning from the state of the art in Table 6. Table 6 reflects the overall performance of the harvesters in terms of bandwidth and NPD. It also provides the figure of merit that corresponds to the product of both (bandwidth x NPD), in order to highlight the ability to recover energy with a strong normalized power density over a wide frequency band. For our VEH, the maximal relative displacement amplitude d with the SC-SECE is evaluated equal to 57 µm. The overall volume is equal to $(H_m + 2d) \times (L_m + L_p) \times B = 719$ mm³. The NPD correspond to 12.0 mW/G²/cm³.

Table 6: State-of-the-art of strongly coupled VEHs associated to electrical resonant frequency tuning

Ref.	[14]	[8]	[5]	[13]	[4]	[3]	**This work**
Material	PZT-5	PZT-5A	PZT-5H	PZN-PT	PMN-PT	PZN-PT	PZN-PT
Coupling k^2	11.5%	16.4 %	14 %	**50 %**	13.5 %	32 %	49.8 %
Q_m	60	91	27	20	80	20	**142**
$k_e^2 Q_m$	7.8	18	4.5	20	12.5	9.41	**140**
Frequency	189 Hz	33.7 Hz	673 Hz	208 Hz	27.5 Hz	98.7 Hz	129 Hz
Volume	1.53 cm³	19.1 cm³	2.49 cm³	6.75 cm³	6.3 cm³	1 cm³	0.719 cm³
Acceleration	2.5 m/s²	0.09 m/s²	9.8 m/s²	1.4 m/s²	0.4 m/s²	0.29 m/s²	0.34 m/s²
Mean Power	5 220 µW	21.1 µW	148 µW	480 µW	93 µW	6 µW	10.4 µW
Technique	R-Tuning	R-tuning	PS-PSSHI	RC-Tuning	FT-SECE	SC-SECE	SC-SECE
Type of power	Extracted	Extracted	Harvested	Extracted	Extracted	Extracted	Extracted
Bandwidth BW	9.3 %	12.8 %	12.8 %	32.7 %	12.4 %	**43.5 %**	36.0 %
NPD	5 250 µW/cm³/G²	**12 320 µW/cm³/G²**	597 µW/cm³/G²	3 560 µW/cm³/G²	8 780 µW/cm³/G²	4 190 µW/cm³/G²	12 029 µW/cm³/G²
NPD × BW	488	1 577	76	1 164	1 089	1 823	**4 318**

The VEHs from the state of the art are represented as a function k^2 and Q_m in Figure 23. Isolines are also represented to show the value of $k_e^2 Q_m$. The height of the ellipses correspond to the frequency bandwidth and the width corresponds to the NPD. The surface of the ellipses quantifies the figure of merit which is the product of the NPD and the bandwidth, also given in Table 6.

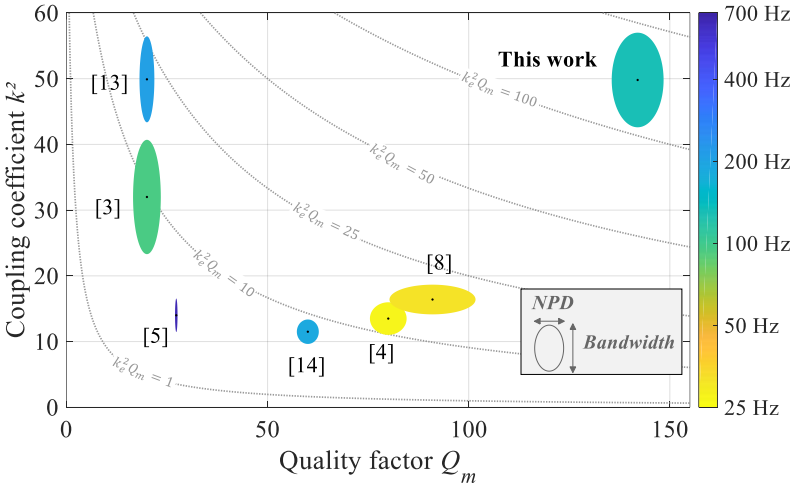

Figure 23: State of the art of strongly coupled VEHs associated with electrical resonant frequency tuning

From Figure 23, it can be noticed that increasing the coupling allows to increase the frequency bandwidth. This can be observed with the wide bandwidth of the devices from [3] and [13] and our device. In the same manner, with the device from [8] and our device, we notice that increasing the quality factor helps to increase the normalized power density.

The performances of the electrical tuning solution are compared to the other broadband and high NPD solutions. Figure 24 represents, to our knowledge, the best VEHs from the state-of-the-art as a function of the NPD and the bandwidth. The values of NPD are given in Table 7.

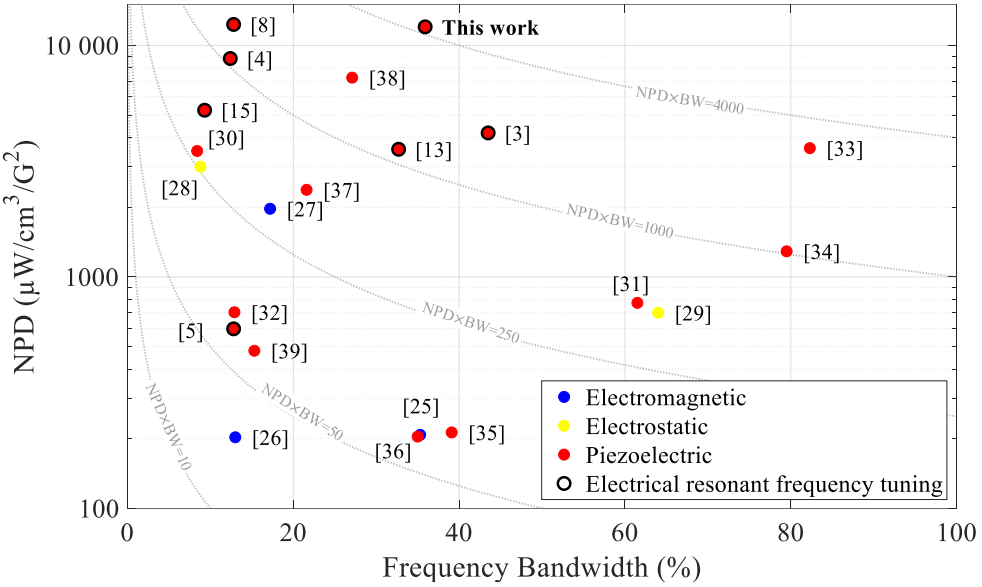

Figure 24: Comparison of the best performing state-of-the-art VEHs. The values of NPD and bandwidths are given in Table 6 and Table 7

Table 7: High performance VEHs with methods different from the electrical resonant frequency tuning. EM, ES, PE hold for electromagnetic, electrostatic and piezoelectric respectively

	Source	Method	Central frequency (Hz)	Acceleration (m/s²)	Power (µW)	Volume (cm³)	NPD (µW/cm³/G²)	Bandwidth	NPD×BW
EM	[25]	Multi-frequency	8.5	5	2010	40.1	208	35.3 %	73
	[26]	Duffing	59.8	9.8	1180	5.8	203	13 %	26
	[27]	Duffing	11	3.94	≈70 000	100.5	1 970	17.2 %	339
ES	[28]	Stoppers	136	0.9	4.95	0.187	2 995	8.8 %	264
	[29]	/	100	0.981	0.08	/	700	64 %	448
PE	[30]	/	155	9.8	95	0,027	3500	8.4 %	294
	[31]	Bistable	5.2	10	105000	130	773	61,5 %	475
	[32]	Duffing	29.4	1	920	125	704	12.9 %	91
	[33]	Bistable	19.4	3	16000	48	3600	82.3 %	2963
	[34]	Bistable	47.1	6	2634	5.46	1290	79.5 %	1026
	[35]	Bistable	11.5	19.6	34000	40	213	39.1 %	83
	[36]	Tristable	4.25	1	44	/	204.5	35 %	72
	[37]	Hardening	2 050 rpm	9.81	78 870	33.15	2 379	21.6 %	514
	[38]	Bistable	37.3	4.7	23 000	12.7	7 258	27.1 %	1967
	[39]	Bistable	97.8	19.62	600	3.12	480	15.3 %	73
	This work		156.9	0.34	10.4	0.719	12 029	36.0 %	4318

With the highest product NPD×BW in Table 6 and Table 7, our VEH offers the best performances of VEHs allowing simultaneously wideband frequency tuning capability and very high NPD. Furthermore, the interesting performances of most the VEHs in Table 7 are obtained thanks to nonlinearities which induce jump phenomenon associated to responses that differ between a forward frequency sweep and a reverse frequency sweep [26,27,31–39]. As their harvested power is strongly dependent on the initial conditions and on the acceleration level, the reported performances in Table 7 may, at some point, be difficult to achieve in real application.

In comparison, the performances of electrical frequency tuning solutions is interesting for applications where the vibrations have a low acceleration level. Furthermore, recent progress has been made in low power integrated circuit that can dynamically and autonomously tune the resonant frequency of strongly coupled VEHs [6]. Our solution offers promising prospects for powering a wireless sensor node with a vibration source whose dominant frequency is variable or for countering the variation of the HEV resonant frequency due to temperature variation or aging.

5. Conclusions

This work presents a method to design high-performance vibration energy harvesters whose resonant frequency can be tune in a large range using electrical resonant frequency tuning. The proposed method allows to design harvesters able to harvest vibration energy over a wide range of frequencies and with high normalized power density.

As the combined maximization of the electromechanical coupling coefficient k^2 and of the mechanical quality factor Q_m are mandatory to increase the harvested power and the resonant frequency tuning capabilities, our present work considers these both aspects for the global design of vibration energy harvesters. An analytical model is developed and studied to provide general guidelines for the design of piezoelectric cantilevers. The analytical expressions of the quality factor Q_m is deduced from material intrinsic losses and the analytical expression of the figure of merit $k_e^2 Q_m$ is for the first time provided in the literature for piezoelectric cantilever with proof masses. Notable findings from the model include:

- soft substrate material should be preferred for maximizing the global electromechanical coupling coefficient of the harvesters,
- a substrate material with high quality factor does not affect much the quality factor Q_m of cantilevers when the substrate thickness is optimized to maximize the coupling coefficient k^2,
- the ratio of the substrate quality factor Q_s and its Young modulus Y_s (i.e. Q_s/Y_s) has a primordial influence on the maximization of $k_e^2 Q_m$,
- an optimal thickness ratio between piezoelectric and substrate materials allows to maximize $k_e^2 Q_m$. For bimorph structure with patches all along the beam, $k_e^2 Q_m$ cannot be higher than the figure of merit of the piezoelectric material $k_{e31}^2 Q_p$

The optimization of the high-performance cantilever is realized thanks to the model, 3D Comsol simulations, loss measurement on materials in the optics of maximizing $k_e^2 Q_m$. Efforts are made to primary maximize k^2 in order to allow large resonant frequency tuning range capabilities and secondary on Q_m in order to maximize the harvested power. A strongly coupled cantilever is therefore realized with PZN-5.5PT [011] and aluminum. Furthermore, our study shows that small manufacturing defects can have a huge impact on k^2 and, therefore, on $k_e^2 Q_m$. Based on experiment under harmonic vibration excitation with output resistive loads, the proposed harvester demonstrates a coupling coefficient k^2 equal to 49.8% and a quality factor of 142 at 0.5 m/s² acceleration amplitude. This represented a $k_e^2 Q_m$ of 140 which is, to our knowledge, the best from the state of the art of piezoelectric vibration energy harvesters. The frequency tuning capabilities of harvester are demonstrated by experiments using the SC-SECE technique at 0.34 m/s². The harvester generates a maximal mean power of 10.4 µW with 36 % relative bandwidth and have a normalized power density of 12.4 mW/g²/cm³. Compared to the state-of-the-art, our harvester provides the best combined performances considering frequency bandwidth and normalized power density.

Since the influence of bending modes higher than the fundamental mode was observed in the experimental voltage response with the SC-SECE technique, future work will focus on understanding the coupling between the vibration modes and the influence of the electrical interface. This work will allow the realization of resonant frequency tuning circuits for the powering of wireless sensors nodes by harvesting vibratory energy of wide frequency band.

Appendix

As shown in (27), $\mathcal{R}_L$ only depends on the strain distribution along the beam given by the *b/a* ratio. *a* and *b* are expressed in (28) and (29) respectively with Γ a coefficient expressed in (30). J_t is the rotary inertia to mass ratio expressed as $J_t = I_t/M_t$.

$$\mathcal{R}_L = \frac{\left(\frac{b}{a}\right)^2 + \left(\frac{b}{a}\right) + \frac{1}{4}}{\left(\frac{b}{a}\right)^2 + \left(\frac{b}{a}\right) + \frac{1}{3}} \tag{27}$$

$$a = \frac{6\left(6\,J_t - 2\sqrt{\Gamma} + 6\,D_T^2 + L_b^2 + 6\,D_T L_b\right)}{L_b^3\left(3\,J_t - \sqrt{\Gamma} + 3\,D_T^2 - L_b^2\right)} \tag{28}$$

$$b = -\frac{6\left(3\,J_t - \sqrt{\Gamma} + 3\,D_T^2 + L_b^2 + 4\,D_T L_b\right)}{L_b^2\left(3\,J_t - \sqrt{\Gamma} + 3\,D_T^2 - L_b^2\right)} \tag{29}$$

$$\Gamma = 9\,D_T^4 + 18\,D_T^3 L_b + 15\,D_T^2 L_b^2 + 18\,D_T^2 J_t + 6\,D_T L_b^3 + 18\,D_T L_b J_t + L_b^4 + 3\,L_b^2 J_t + 9\,J_t^2 \tag{30}$$

The optimization of $\mathcal{R}_L$ has already been discussed in the previous paper [8]. $\mathcal{R}_L$ and the strain distribution along the beam can be improved with a long proof mass. Indeed, a length of mass L_m equal to the length of the beam L_b leads to a value of $\mathcal{R}_L$ larger than 12/13 (i.e. 0.92) whatever the height of the mass.

References

[1] Priya S, Song H-C, Zhou Y, Varghese R, Chopra A, Kim S-G, Kanno I, Wu L, Ha D S, Ryu J and Polcawich R G 2019 A Review on Piezoelectric Energy Harvesting: Materials, Methods, and Circuits *Energy Harvesting and Systems* **4** 3–39

[2] Morel A, Brenes A, Gibus D, Lefeuvre E, Gasnier P, Pillonnet G and Badel A 2022 A comparative study of electrical interfaces for tunable piezoelectric vibration energy harvesting *Smart Mater. Struct.* **31** 045016

[3] Morel A, Pillonnet G, Gasnier P, Lefeuvre E and Badel A 2018 Frequency tuning of piezoelectric energy harvesters thanks to a short-circuit synchronous electric charge extraction *Smart Mater. Struct.* **28** 025009

[4] Brenes A, Morel A, Gibus D, Yoo C-S, Gasnier P, Lefeuvre E and Badel A 2020 Large-bandwidth piezoelectric energy harvesting with frequency-tuning synchronized electric charge extraction *Sensors and Actuators A: Physical* **302** 111759

[5] Zhao S, Radhakrishna U, Lang J and Buss D 2021 Low-Voltage Broadband Piezoelectric Vibration Energy Harvesting Enabled by a Highly-Coupled Harvester and Tunable PSSHI Circuit *Smart Mater. Struct.*

[6] Morel A, Quelen A, Berlitz C A, Gibus D, Gasnier P, Badel A and Pillonnet G 2020 Fast-Convergence Self-Adjusting SECE Circuit With Tunable Short-Circuit Duration Exhibiting 368% Bandwidth Improvement *IEEE Solid-State Circuits Letters* **3** 222–5

[7] Cai Y and Manoli Y 2018 A piezoelectric energy-harvesting interface circuit with fully autonomous conjugate impedance matching, 156% extended bandwidth, and 0.38μW power consumption *2018 IEEE International Solid - State Circuits Conference - (ISSCC)* 2018 IEEE International Solid - State Circuits Conference - (ISSCC) pp 148–50

[8] Gibus D, Gasnier P, Morel A, Formosa F, Charleux L, Boisseau S, Pillonnet G, Berlitz C A, Quelen A and Badel A 2020 Strongly coupled piezoelectric cantilevers for broadband vibration energy harvesting *Applied Energy* **277** 115518

[9] Badel A and Lefeuvre E 2014 Wideband Piezoelectric Energy Harvester Tuned Through its Electronic Interface Circuit *Journal of Physics: Conference Series* **557** 012115

[10] Wu W-J, Chen Y-Y, Lee B-S, He J-J and Peng Y-T 2006 Tunable resonant frequency power harvesting devices Smart Structures and Materials ed W W Clark, M Ahmadian and A Lumsdaine (San Diego, CA) p 61690A

[11] Charnegie D 2007 Frequency Tuning Concepts For Piezoelectric Cantilever Beams And Plates For Energy Harvesting

[12] Seddik B A, Despesse G and Defay E 2012 Wideband mechanical energy harvester based on piezoelectric longitudinal mode *New Circuits and Systems Conference (NEWCAS), 2012 IEEE 10th International* (IEEE) pp 453–6

[13] Ahmed-Seddik B, Despesse G, Boisseau S and Defay E 2013 Self-powered resonant frequency tuning for Piezoelectric Vibration Energy Harvesters *Journal of Physics: Conference Series* **476** 012069

[14] Kuang Y, Chew Z J and Zhu M 2020 Strongly coupled piezoelectric energy harvesters: Finite element modelling and experimental validation *Energy Conversion and Management* **213** 112855

[15] Badel A and Lefeuvre E 2016 Nonlinear Conditioning Circuits for Piezoelectric Energy Harvesters *Nonlinearity in Energy Harvesting Systems: Micro- and Nanoscale Applications* ed E Blokhina, A El Aroudi, E Alarcon and D Galayko (Cham: Springer International Publishing) pp 321–59

[16] Morel A, Badel A, Grézaud R, Gasnier P, Despesse G and Pillonnet G 2019 Resistive and reactive loads' influences on highly coupled piezoelectric generators for wideband vibrations energy harvesting *Journal of Intelligent Material Systems and Structures* **30** 386–99

[17] Shu Y C and Lien I C 2006 Efficiency of energy conversion for a piezoelectric power harvesting system *J. Micromech. Microeng.* **16** 2429–38

[18] Lim Y Y and Soh C K 2014 Towards more accurate numerical modeling of impedance based high frequency harmonic vibration *Smart Mater. Struct.* **23** 035017

[19] Liu G, Zhang S, Jiang W and Cao W 2015 Losses in ferroelectric materials *Materials Science and Engineering: R: Reports* **89** 1–48

[20] Lei A, Xu R, Borregaard L M, Guizzetti M, Hansen O and Thomsen E V 2014 Impedance Based Characterization of a High-Coupled Screen Printed PZT Thick Film Unimorph Energy Harvester *Journal of Microelectromechanical Systems* **23** 842–54

[21] Clementi G, Ouhabaz M, Margueron S, Suarez M A, Bassignot F, Gauthier-Manuel L, Belharet D, Dulmet B and Bartasyte A 2021 Highly coupled and low frequency vibrational energy harvester using lithium niobate on silicon *Appl. Phys. Lett.* **119** 013904

[22] Anon 2020 | Microfine

[23] Gibus D, Gasnier P, Morel A, Garraud N and Badel A 2022 Non-linear losses study in strongly coupled piezoelectric device for broadband energy harvesting *Mechanical Systems and Signal Processing* **165** 108370

[24] Leadenham S 2015 *Advanced concepts in nonlinear piezoelectric energy harvesting: intentionally designed, inherently present, and circuit nonlinearities* PhD Thesis (Georgia Institute of Technology)

[25] Foisal A R Md, Hong C and Chung G-S 2012 Multi-frequency electromagnetic energy harvester using a magnetic spring cantilever *Sensors and Actuators A: Physical* **182** 106–13

[26] Roy S, Podder P and Mallick D 2016 Nonlinear Energy Harvesting Using Electromagnetic Transduction for Wide Bandwidth *IEEE Magnetics Letters* **7** 1–4

[27] Aldawood G, Nguyen H T and Bardaweel H 2019 High power density spring-assisted nonlinear electromagnetic vibration energy harvester for low base-accelerations *Applied Energy* **253** 113546

[28] Zhang Y, Wang T, Luo A, Hu Y, Li X and Wang F 2018 Micro electrostatic energy harvester with both broad bandwidth and high normalized power density *Applied Energy* **212** 362–71

[29] Honma H, Tohyama Y and Toshiyoshi H 2021 A Short-Stroke Electrostatic Vibrational Energy Harvester with Extended Bandwidth and Sensitivity *2021 21st International Conference on Solid-State Sensors, Actuators and Microsystems (Transducers)* 2021 21st International Conference on Solid-State Sensors, Actuators and Microsystems (Transducers) pp 132–5

[30] Aktakka E E and Najafi K 2014 A Micro Inertial Energy Harvesting Platform With Self-Supplied Power Management Circuit for Autonomous Wireless Sensor Nodes *IEEE Journal of Solid-State Circuits* **49** 2017–29

[31] Mann B P and Owens B A 2010 Investigations of a nonlinear energy harvester with a bistable potential well *Journal of Sound and Vibration* **329** 1215–26

[32] Sebald G, Kuwano H, Guyomar D and Ducharne B 2011 Simulation of a Duffing oscillator for broadband piezoelectric energy harvesting *Smart Mater. Struct.* **20** 075022

[33] Liu W Q, Badel A, Formosa F, Wu Y P and Agbossou A 2013 Novel piezoelectric bistable oscillator architecture for wideband vibration energy harvesting *Smart Mater. Struct.* **22** 035013

[34] Liu W, Badel A, Formosa F, Wu Y, Bencheikh N and Agbossou A 2015 A wideband integrated piezoelectric bistable generator: Experimental performance evaluation and potential for real environmental vibrations *Journal of Intelligent Material Systems and Structures* **26** 872–7

[35] Arrieta A F, Hagedorn P, Erturk A and Inman D J 2010 A piezoelectric bistable plate for nonlinear broadband energy harvesting *Appl. Phys. Lett.* **97** 104102

[36] Zou D, Liu G, Rao Z, Tan T, Zhang W and Liao W-H 2021 Design of a multi-stable piezoelectric energy harvester with programmable equilibrium point configurations *Applied Energy* **302** 117585

[37] Wang Y, Yang Z, Li P, Cao D, Huang W and Inman D J 2020 Energy harvesting for jet engine monitoring *Nano Energy* **75** 104853

[38] Li H T, Qin W Y, Zu J and Yang Z 2018 Modeling and experimental validation of a buckled compressive-mode piezoelectric energy harvester *Nonlinear Dyn* **92** 1761–80

[39] Yi Z, Hu Y, Ji B, Liu J and Yang B 2018 Broad bandwidth piezoelectric energy harvester by a flexible buckled bridge *Appl. Phys. Lett.* **113** 183901